*Article*

# Porous Ruthenium–Tungsten–Zinc Nanocages for Efficient Electrocatalytic Hydrogen Oxidation Reaction in Alkali

**Xiandi Sun** *,†, **Zhiyuan Cheng** †, **Hang Liu, Siyu Chen and Ya-Rong Zheng**

Anhui Province Key Laboratory of Value-Added Catalytic Conversion and Reaction Engineering, Anhui Province Engineering Research Center of Flexible and Intelligent Materials, School of Chemistry and Chemical Engineering, Hefei University of Technology, Hefei 230009, China; zhiyuanc@mail.hfut.edu.cn (Z.C.); hangliu@mail.hfut.edu.cn (H.L.); chensy@mail.hfut.edu.cn (S.C.); yrzh@mail.hfut.edu.cn (Y.-R.Z.)
* Correspondence: sxd492@mail.hfut.edu.cn
† These authors contributed equally to this work.

**Abstract:** With the rapid development of anion exchange membrane technology and the availability of high-performance non-noble metal cathode catalysts in alkaline media, the commercialization of anion exchange membrane fuel cells has become feasible. Currently, anode materials for alkaline anion-exchange membrane fuel cells still rely on platinum-based catalysts, posing a challenge to the development of efficient low-Pt or Pt-free catalysts. Low-cost ruthenium-based anodes are being considered as alternatives to platinum. However, they still suffer from stability issues and strong oxophilicity. Here, we employ a metal–organic framework compound as a template to construct three-dimensional porous ruthenium–tungsten–zinc nanocages via solvothermal and high-temperature pyrolysis methods. The experimental results demonstrate that this porous ruthenium–tungsten–zinc nanocage with an electrochemical surface area of 116 m$^2$ g$^{-1}$ exhibits excellent catalytic activity for hydrogen oxidation reaction in alkali, with a kinetic density 1.82 times and a mass activity 8.18 times higher than that of commercial Pt/C, and a good catalytic stability, showing no obvious degradation of the current density after continuous operation for 10,000 s. These findings suggest that the developed catalyst holds promise for use in alkaline anion-exchange membrane fuel cells.

**Keywords:** anion-exchange membrane fuel cell; hydrogen oxidation reaction; metal–organic frameworks; porous nanocages

## 1. Introduction

In recent years, hydrogen energy has received extensive attention as a potential alternative to fossil fuels due to its high energy density of up to 140 MJ Kg$^{-1}$, as well as its clean and environmentally friendly characteristics [1]. Hydrogen fuel cells are known for their high energy conversion efficiency and zero-carbon emissions, making them one of the most competitive technologies for hydrogen utilization [2]. Fuel cells are classified into five categories based on the type of electrolyte and the operating conditions, including proton exchange membrane fuel cells (PEMFCs), anion exchange membrane fuel cells (AEMFC), phosphoric acid fuel cells, molten carbonate fuel cells, and solid oxide fuel cells [3]. So far, PEMFCs have been at the forefront of cutting-edge energy conversion technologies used in various applications, such as automobiles, communications, and aerospace. However, PEMFCs require platinum (Pt)-based electrocatalysts, acid-resistant electric pile hardware, and perfluorinated membranes, resulting in high production costs [4]. The AEMFC represents a highly efficient and environmentally friendly power generation technology. It is regarded as a new-generation energy power system due to its high cell efficiency, excellent catalyst stability, and flexible fuel selectivity. Anion-exchange membranes are seen as the next generation of cost-effective fuel cells because they can use efficient, non-precious metal catalysts in the cathodic oxygen reduction reaction, significantly reducing fuel cell costs [5]. However, the kinetics of Pt group metals required for anode hydrogen oxidation

reactions (HORs) in an alkaline media are 2–3 orders of magnitude lower than those in an acidic media. Therefore, improving the performance of noble metal catalysts or developing efficient low-cost alkaline HOR catalysts remains a major challenge [6,7].

Ruthenium (Ru) possesses a similar hydrogen binding energy to Pt, but is much less expensive than Pt, making it a potential substitute to Pt for alkaline HORs [8,9]. However, Ru exhibits oxyphilic properties at anodic potentials above 0.1 V compared to a reversible hydrogen electrode (RHE), leading to a decreased electrochemical HOR performance [10]. Several strategies have recently been developed to enhance the performance of Ru-based catalysts, including compositional effects [11–13], carrier effects [14–17], size effects [18,19], and structural effects [20,21]. In the case of loaded catalysts, they are usually overlooked when the particles are loaded or embedded in the carrier, which may result in underutilization of the active sites [22,23].

Metal–organic frameworks (MOFs), three-dimensional ordered porous structure materials, have garnered significant attention due to their high specific surface area and controllable porous structure [24]. Furthermore, MOF structures offer the advantages of being easily designed and modified, enabling the direct synthesis of various functional materials derived from MOFs. MOF-derived catalysts often possess hollow structures, facilitating mass transfer and intermediate diffusion, thus improving catalytic performance [25–28]. For example, Ma et al. [29] used octahedral zeolitic imidazolate framework-8 (ZIF-8) as a template to construct sub-2 nm RuMo-anchored hollow carbon catalysts, exhibiting a high activity for alkaline HOR, with a mass activity of 3.83 A $mg_{Ru}^{-1}$, which is 25 times higher than that of commercial Ru/C. Qiu et al. [30] reported a general method for synthesizing binary, ternary, and high-entropy nanoparticles using a 2D MOF-assisted pyrolysis-replacement alloying technique. The developed $Co_{0.2}Ru_{0.7}Pt_{0.1}$/PNC nanosheets exhibited a mass activity as high as 1.84 A $mg^{-1}$ at an overpotential of 50 mV. Therefore, constructing high surface area catalysts and improving their exposure rates are the key factors for enhancing the alkaline HOR performance.

Here, we synthesize a three-dimensional hollow porous ruthenium–tungsten–zinc (Ru-W-Zn-O) nanocage through a hydrothermal reaction and high-temperature pyrolysis processes. The optimized $Ru_1W_{0.14}Zn_{1.47}O_y$ catalyst exhibits an enhanced HOR performance in alkaline conditions compared to commercial Pt/C and Ru/C. Specifically, the kinetic current densities ($j_k$) were 1.82 and 1.04 times higher than those of commercial Pt/C and Ru/C, respectively. After a constant voltage test for 10,000 s, the current density of $Ru_1W_{0.14}Zn_{1.47}O_x$ shows no significant decay. These fundings make $Ru_1W_{0.14}Zn_{1.47}O_x$ a promising candidate for alkaline AEMFC anode materials.

## 2. Materials and Methods

### 2.1. Materials

Zn $(NO_3)_2 \cdot 6H_2O$, cetyltrimethylammonium bromide (CTAB), potassium hydroxide (KOH), isopropanol, and methanol were purchased from Sinopharm (Shanghai, China), and 2-methyl imidazole was purchased from Beijing Jin Ming Biotechnology Co., Ltd. (Beijing, China). $RuCl_3 \cdot xH_2O$, Ru/C (20 wt%), and $Na_2WO_4$ were purchased from Macklin (Shanghai, China). Pt/C (20 wt%) was purchased from Suzhou Sinero Technology Co., Ltd. (Suzhou, China). Nafion®117 solution was purchased from Sigma-Aldrich (St. Louis, MO, USA) (~5% in a mixture of lower aliphatic alcohols and water, containing 15~20% water). All reagents were analytically pure and used as received without further purification.

### 2.2. Material Characterization

Transmission electron microscopy (TEM) and Field-Emission Scanning Electron Microscopy (SEM) images were obtained from a Hitachi H7700 and SU8020 (Tokyo, Japan) at an accelerating voltage of 100 KV. The data of high-revolution TEM images and EDS elemental mapping were obtained from a JEM-2100F (Tokyo, Japan). The catalyst solution was applied onto 300-mesh copper grids coated with formvar/carbon support film (Beijing Zhongjing Key Technology Co., Ltd., Beijing, China). The powder X-ray diffraction

(XRD) patterns were obtained on Philips X'Pert Pro Super with a Cu Ka radiation source ($\lambda$ = 1.541841 Å). X-ray photoelectron spectra (XPS) were measured using an Al K$\alpha$ radiation source on a Thermo Fisher ESCALAB 250Xi (Waltham, MA, USA). The peak shifts caused by apparent charging were calibrated using the carbon C 1$s$ peak set to 284.8 eV. All spectra were collected in ambient conditions. All electrochemical performances were conducted with an electrochemical workstation (Autolab, Metrohm, Herisau, Switzerland). The noble metal mass content of Ru in $Ru_1W_{0.14}Zn_{1.47}O_x$ and $RuZnO_x$ nanocages were determined by inductively coupled plasma-Mass Spectrometry (ICP-MS, Agilent Technologies 7500 series, Santa Clara, CA, USA).

*2.3. Methods*

2.3.1. Preparation of ZIF-8

In a typical preparation, 1.22 mmol of Zn $(NO_3)_2 \cdot 6H_2O$ was dissolved in 12.5 mL of deionized water and stirred at 350 rpm. Separately, 70.64 mmol of 2-methyl imidazole and 1.22 mmol of CTAB were mixed with 87.5 mL deionized water. The Zn $(NO_3)_2 \cdot 6H_2O$ solution was then quickly injected into the second solution and stirred continuously for 5 min. The above operations were conducted at room temperature, followed by standing for several hours to obtain a uniformly dispersed ZIF-8 solution.

2.3.2. Synthesis of $Ru_1W_{0.14}Zn_{1.47}O_x$ Nanocage

As is typical for the synthesis of nanocages, 8 mL of the white ZIF-8 solution was taken for centrifugation, and the precipitate was rinsed with methanol several times. Then, 3 mL of deionized water was added to the precipitate and dispersed by ultrasound. Meanwhile, 10 mg of $RuCl_3 \cdot xH_2O$ and 2 mg of $Na_2WO_4$ were dispersed in a mixed solution of 2 mL deionized water and 1 mL methanol. The resulting solution was then injected into the ZIF-8 suspension and thoroughly mixed by stirring for 30 min. After that, the mixture was transferred into a 20 mL Teflon-lined autoclave and heated at 80 °C for 2 h. Finally, the resulting sample (denoted as RuW-2@ZIF-8) was then placed in a porcelain boat and calcined in a reducing gas, $H_2/Ar$ (95%). The temperature was raised to 300 °C at a heating rate of 10 °C/min and maintained for 2 h. After cooling to room temperature, the $Ru_1W_{0.14}Zn_{1.47}O_x$ nanocage was finally obtained. Soon afterwards, using 6 mg of W precursor while Ru was unchanged (denoted as RuW-6@ZIF-8) as the precatalyst, the $Ru_1W_{0.33}Zn_{1.14}O_x$ nanocage could be obtained. The catalyst $RuZn_xO_y$ was obtained without using W precursor and Ru was kept unchanged. The atomic ratio between Ru, W, and Zn was obtained based on the XPS analysis.

2.3.3. Electrochemical Measurements

As is generally carried out for electrochemical measurements, 1 mg of the developed catalyst was added to 400 μL isopropanol, while 1 mg of carbon black was added to 390 μL of isopropanol and 10 μL of Nafion (5 wt%) solution. The mixture was continuously ultrasonicated for several hours until a homogeneous ink formed. Then, 15 μL of catalyst ink was evenly pipetted onto the glassy carbon working electrode. The catalyst loading on the working electrode was 0.19 mg/cm$^2$.

Electrochemical tests were performed using a three-electrode system. The working electrode was a rotating disk electrode with a disk area of 0.196 cm$^2$ and a rotation speed ranging from 400 to 2500 rpm. A saturated calomel electrode (SCE) and a graphite carbon electrode were used as the reference electrode and the counter electrode, respectively. Prior to testing, the 0.1 M KOH electrolyte was saturated with $H_2$. The catalysts were first tested using cyclic voltammetry (CV) followed by linear sweep voltammetry (LSV) to ensure a quick attainment of steady state. The voltage range of CV was −0.05~0.2 V vs. RHE, with a scan rate of 10 mV s$^{-1}$. For LSV, the scan rate was 1 mV s$^{-1}$, and the rotation speed was 1600 rpm. The stability test of $Ru_1W_{0.14}Zn_{1.47}O_x$ was performed using a chronoamperometry test (CA) at a constant potential of 50 mV vs. RHE in $H_2$-saturated

0.1 M KOH. Unless otherwise mentioned, the potentials in this work were converted to the reversible hydrogen electrode by the equation:

$$E_{\mathrm{RHE}} = E_{\mathrm{SCE}} + 0.059 \times \mathrm{pH} + 0.253$$

Due to the fact that Ru-based materials tend to absorb OH* in the hydrogen underpotential deposition (UPD) area. In this work, the Cu UPD method was employed to determine the electrochemical active surface areas (ECSAs) of Ru-based catalysts. The catalysts were subjected to multiple cycles of scanning, ranging from 0 to 0.7 V vs. RHE in order to obtain a stable CV curve as a background measurement in an Ar-saturated 0.1 M $H_2SO_4$ solution, with a scan rate of 10 mV s$^{-1}$. When the deposition of Cu occurs at 0.3 V vs. RHE for a duration of 100 s, the stripping of Cu-UPD commences at potentials ranging from 0.3–0.7 V vs. RHE in an Ar-saturated 0.1M $H_2SO_4$ solution containing 2 mM $CuSO_4$, with a scanning rate of 10 mV s$^{-1}$. The value of ECSA (cm$^2$ g$^{-1}$) can be calculated using the equation:

$$\mathrm{ECSA}\left(\frac{\mathrm{cm}^2_{\mathrm{metal}}}{\mathrm{g}_{\mathrm{metal}}}\right) = \frac{Q_{\mathrm{Cu}}}{m_{\mathrm{metal}} \cdot 420\ \mu\mathrm{C\ cm}^{-2}}$$

where $Q_{\mathrm{Cu}}$ is the measured integral charge, $m_{\mathrm{metal}}$ is the mass loading of metals on the electrode, 420 μC cm$^{-2}_{\mathrm{metal}}$ is the surface charge density which is assumed for a monolayer adsorption of Cu-UPD on metal.

After LSV test, electrochemical impedance spectroscopy (EIS) was performed over a frequency range from 200 kHz to 0.1 kHz with a voltage perturbation of 10 mV. The potential after *iR* correction is calculated using the equation:

$$E_{iR} = E - iR$$

where *E* and *R* correspond to the measured potential and the solution resistance, respectively. The kinetic current density ($j_k$) can be obtained by the Koutecky–Levich equation:

$$\frac{1}{j} = \frac{1}{j_k} + \frac{1}{j_d} = \frac{1}{j_k} + \frac{1}{Bc_0 w^{1/2}}$$

where $j$, $j_d$, $B$, $c_0$, and $\omega$ represent the measured current, the diffusional current, the Levich constant, the solubility of $H_2$ ($7.33 \times 10^{-4}$ mol L$^{-1}$), and the rotating speed, respectively. The exchange current density ($j_0$) could be obtained by the Butler–Volmer (B-V) equation:

$$j_k = j_0\left[e^{\frac{\alpha F}{RT}\eta} - e^{\frac{-(1-\alpha)F}{RT}\eta}\right]$$

where $\alpha$, $\eta$, $R$, $T$, and $F$ represent the transfer coefficient, the overpotential, the molar gas constant (8.314 J mol$^{-1}$ K$^{-1}$), the operating temperature, and the Faraday constant, respectively. $j_0$ could be also obtained from the approximate B-V equation:

$$j = j_0 \frac{\eta F}{RT}$$

## 3. Results and Discussion

### 3.1. Catalyst Synthesis and Characterization

We fabricated the $Ru_1W_{0.14}Zn_{1.47}O_x$ nanocage through a two-step process involving hydrothermal and calcination treatments. ZIF-8 was first prepared as the template as detailed in the Methods section. The morphology of the pure ZIF-8 was imaged by TEM, showing a cubic structure with an average size of approximately 100 nm. Furthermore, the TEM images demonstrate that ZIF-8 was uniformly distributed on the copper grid without any agglomeration (Figure 1a). To prepare the Ru-W-Zn-O nanocomposites, $RuCl_3 \cdot xH_2O$ and $Na_2WO_4$ were used as the Ru and W precursors, respectively. Different ratios of Ru/W were applied during the hydrothermal reaction to control the compositions. After

introducing Ru or W ions, ZIF-8 underwent hydrolysis during the hydrothermal treatment, leading to the formation of the hollow nanocage structure, as shown in Figure 1b–d, with Ru and W confined in the substrate. Compared to Ru@ZIF-8 (Figure 1b), the relatively lighter contrast of the hollow structures of RuW@ZIF-8 (Figure 1c,d), indicating the introduction of W might accelerate the replacement of Zn and creating a favorable structure for further electrochemical investigation. To obtain the metallic Ru, which was crucial for electrocatalytic HOR, the precatalysts were subsequently annealed at 300 °C under $Ar/H_2$ (5%) atmosphere and kept at this temperature for 2 h. The atomic ratios of the Ru-W-Zn-O catalysts after annealing were confirmed by XPS analysis. After annealing, ZIF-8 still shows the cubic structure (Figure 1e). In contrast, $RuZn_xO_y$, $Ru_1W_{0.14}Zn_{1.47}O_x$, and $Ru_1W_{0.33}Zn_{1.14}O_x$ catalysts corresponding to Ru@ZIF-8, RuW-2@ZIF8, and RuW-6@ZIF-8 precatalysts, respectively, maintain the pristine hollow structure without any aggregations or collapses. Moreover, the high-temperature treatment also generated pores on the nanocages, which could facilitate $H_2$ transfer and improve the electrocatalytic performance (Figure 1f,g). The SEM images of the annealed samples at different magnifications also demonstrated that the catalysts retained their cubic structure (Figure 2a–f).
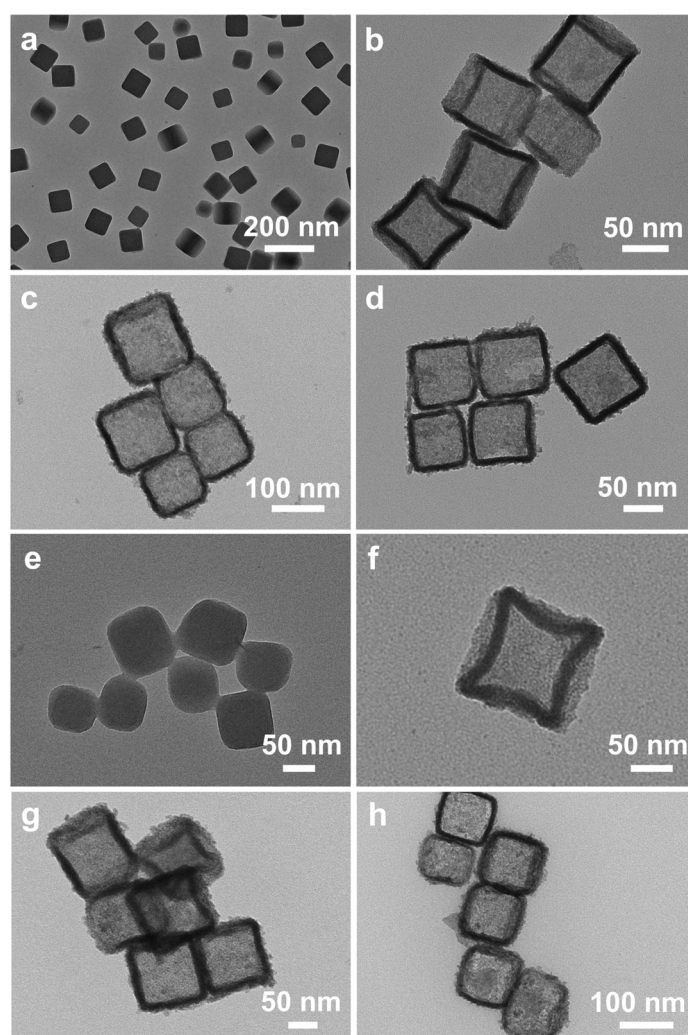


**Figure 1.** Morphology characterization. (**a**–**d**) TEM images of as-prepared (**a**) ZIF-8, precatalysts of (**b**) Ru@ZIF-8, (**c**) RuW-2@ZIF-8, and (**d**) RuW-6@ZIF-8, respectively. (**e**,**f**) TEM images of (**e**) ZIF-8 after annealing, (**f**) $RuZn_xO_y$, (**g**) $Ru_1W_{0.14}Zn_{1.47}O_x$, and (**h**) $Ru_1W_{0.33}Zn_{1.14}O_x$, respectively.
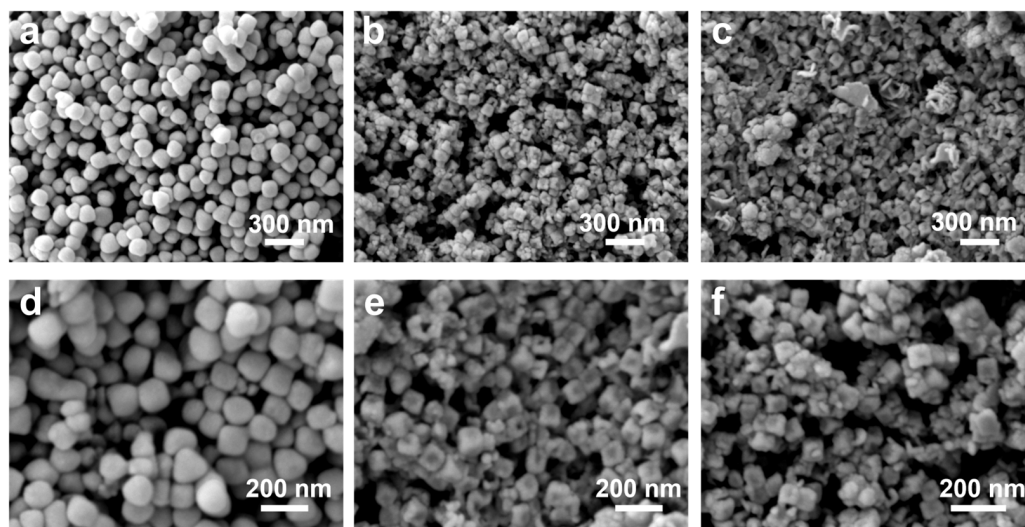
**Figure 2.** SEM images of (**a**,**d**) ZIF-8 after annealing, (**b**,**e**) $Ru_1W_{0.14}Zn_{1.47}O_x$, and (**c**,**f**) $Ru_1W_{0.33}Zn_{1.14}O_x$.

We further conducted XRD characterization to investigate the phase structures of the catalysts. After hydrothermal and annealing treatments, ZIF-8 retained its pristine structure (Figure 3a). The XRD pattern of $RuZn_xO_y$ reveals the presence of ZnO impurity and the hexagonal close-packed Ru (*h*-Ru) phase (JCPDS No. 06-0663). In contrast, after the induction of W, the peaks of ZnO impurities are absent, indicating that Ru-W-Zn-O composites tend to exhibit amorphous structures (Figure 3b). The $Ru_1W_{0.14}Zn_{1.47}O_x$ catalyst shows a broad peak at approximately 42°, which could be assigned to *h*-Ru. However, with increasing W content, the characteristic peaks of *h*-Ru disappear and obvious diffraction peaks of tungsten oxide are observed, which could be attributed to the highly dispersion of W within the nanocomposites.
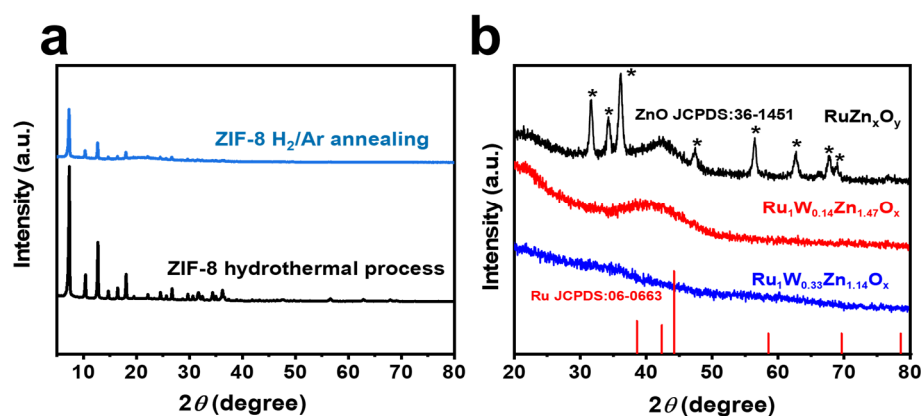


**Figure 3.** XRD patterns of (**a**) ZIF-8 with different treatment ways, (**b**) $RuZn_xO_y$, $Ru_1W_{0.33}Zn_{1.14}O_x$ and $Ru_1W_{0.14}Zn_{1.47}O_x$.

The high-resolution TEM (HRTEM) images were employed to investigate the atomic lattice of the catalysts. Figure 4a,b show that both $RuZn_xO_y$ and $Ru_1W_{0.14}Zn_{1.47}O_x$ nanocages retain a size of approximately 100 nm. These nanocages are composed of numerous nanoparticles and exhibit porous structures. In the HRTEM image of $RuZn_xO_y$ (Figure 4c), the lattice distances of 2.12 Å and 2.65 Å are ascribed to h-Ru (0002) and ZnO (0002) facets, respectively. Ru nanoparticles, with a size ranging from 2 to 5 nm, are seen to be well distributed on the substrate. However, continuous lattice fringes of ZnO are absent from the $Ru_1W_{0.14}Zn_{1.47}O_x$ catalyst after the introduction of W (Figure 4d), and the size of the Ru nanoparticles decreased to approximately 1~2 nm, which is consistent with the XRD

results. Additionally, EDS elemental mapping and line-scanning analysis (Figure 4e–g) demonstrate that Ru, W, and Zn are evenly distributed in the nanocages.
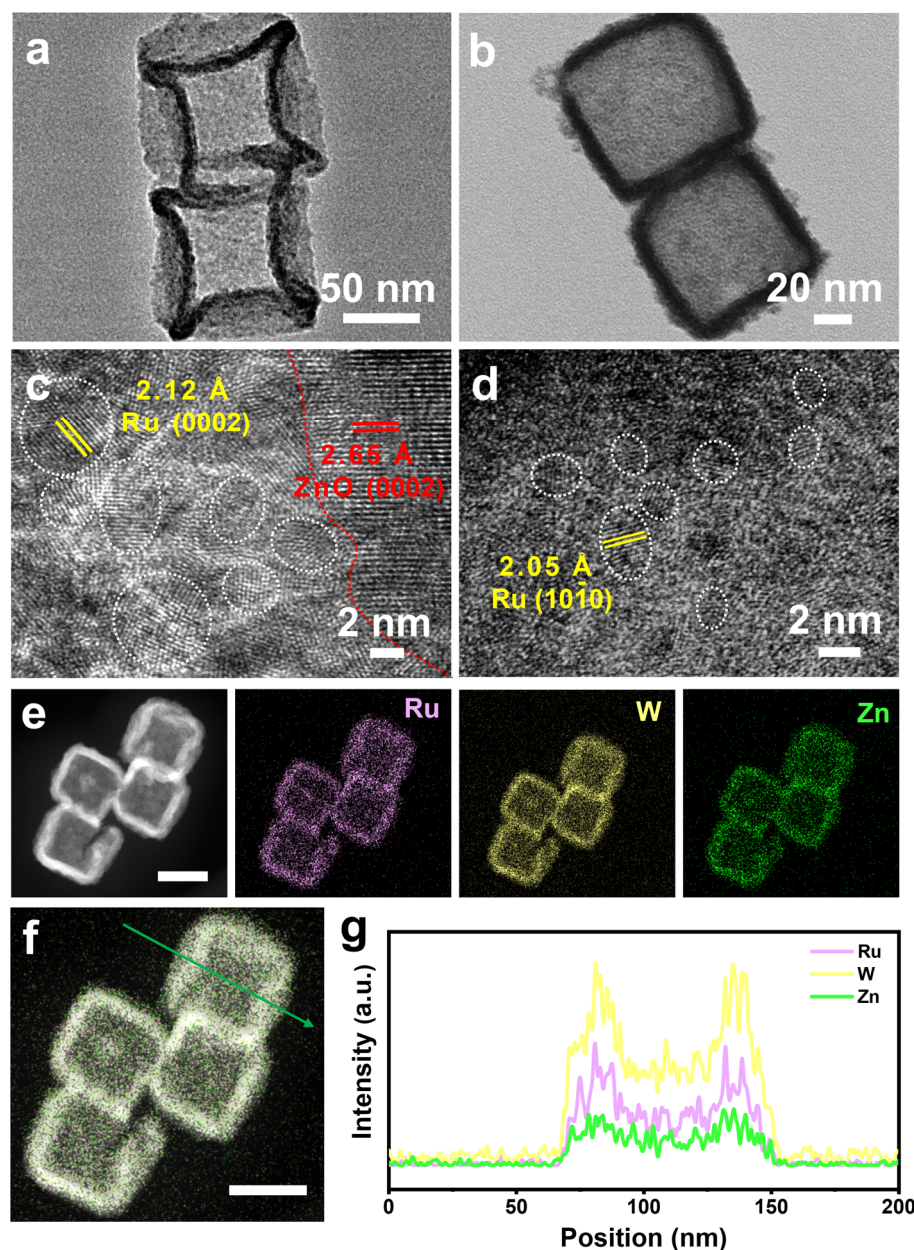


**Figure 4.** TEM images of (**a**) $RuZn_xO_y$ and (**b**) $Ru_1W_{0.14}Zn_{1.47}O_x$, respectively. HRTEM images of (**c**) $RuZn_xO_y$ and (**d**) $Ru_1W_{0.14}Zn_{1.47}O_x$, respectively. (**e**) The EDS elemental mapping analysis of $Ru_1W_{0.14}Zn_{1.47}O_x$. Scale bar: 50 nm. (**f,g**) EDX line-scanning profile of $Ru_1W_{0.14}Zn_{1.47}O_x$ catalyst. Scale bar: 50 nm.

We further conducted XPS analysis to characterize the composition and oxidation state of the catalyst. The XPS survey spectrum of $RuZn_xO_y$ indicates the presence of Ru, Zn, C, and O elements. $Ru_1W_{0.14}Zn_{1.47}O_x$ and $Ru_1W_{0.33}Zn_{1.14}O_x$ exhibit an additional characteristic peak of W compared to $RuZn_xO_y$, indicating successful W and Ru doping (Figure 5). The Ru $3p$ was selected to investigate the valence state of Ru since the binding energies of Ru $3d$ overlap with those C $1s$ [31]. The high-resolution XPS spectra of Ru $3p$ of $RuZn_xO_y$ and $Ru_1W_{0.14}Zn_{1.47}O_x$ after annealing in $H_2/Ar$ atmosphere (Figure 6a) exhibit two peaks at 461.69 and 461.38 eV, corresponding to metallic Ru [32]. The binding energy of the Ru $3p$ in the $Ru_1W_{0.14}Zn_{1.47}O_x$ catalyst is positively shifted compared to

$RuZn_xO_y$, indicating a modification of the electronic structure of Ru due to the introduction of W. The electron transfer between the active site of the Ru and other atoms can modulate the d-band structure of Ru and optimize the binding ability between H* and Ru, thus enhancing the HOR performance. The high-resolution W 4*f* spectrum of $Ru_1W_{0.14}Zn_{1.47}O_x$ (Figure 6b) shows peaks at 37.31 eV and 35.27 eV corresponding to W-O, and at 33.94 eV and 31.54 eV corresponding to W-C [32]. However, $Ru_1W_{0.33}Zn_{1.14}O_x$ only shows peaks at 37.63 and 35.4 eV corresponding to W-O. As shown in Figure 6c, the peaks at 1021.94 and 1022.15 eV corresponding to Zn $2p_{3/2}$, and those at 1044.86 and 1045.19 eV corresponding to Zn $2p_{1/2}$, indicating the presence of $Zn^{2+}$. Figure 6d shows that the peaks located at 531.45 and 531.71 eV corresponding to C=O, and those at 530.02 and 530.40 eV corresponding to W/Zn-O, demonstrate the formation of oxidized W and Zn [33]. These results confirm that Ru remains the metallic state in the developed $RuZn_xO_y$, $Ru_1W_{0.14}Zn_{1.47}O_x$, and $Ru_1W_{0.33}Zn_{1.14}O_x$ catalysts, and the slight shift in Ru 3*p* between $RuZn_xO_y$ and W-doped composites is attributed to the charge transfer effect, which can optimize the electronic structure of the active sites.
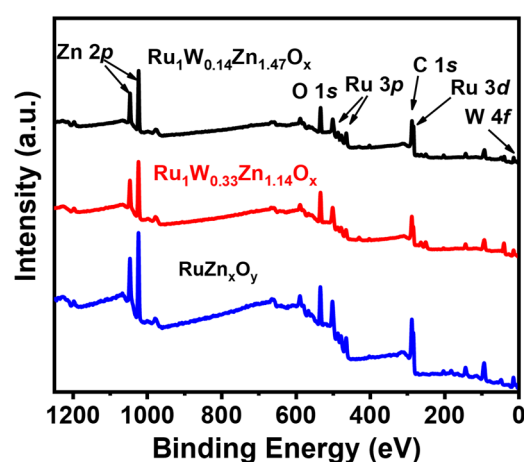


**Figure 5.** XPS survey spectra of $RuZn_xO_y$, $Ru_1W_{0.14}Zn_{1.47}O_x$, and $Ru_1W_{0.33}Zn_{1.14}O_x$.
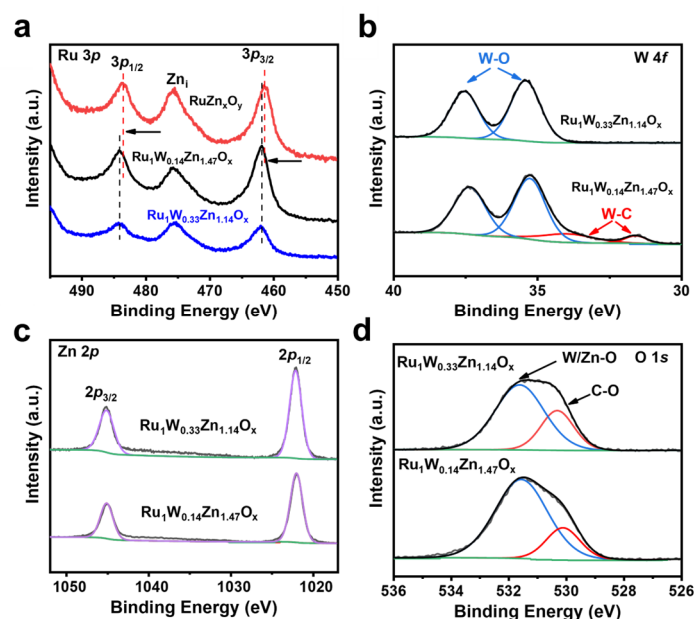


**Figure 6.** High-resolution XPS spectra of (**a**) Ru 3*p* of $RuZn_xO_y$, $Ru_1W_{0.14}Zn_{1.47}O_x$ and $Ru_1W_{0.33}Zn_{1.14}O_x$. High-resolution XPS spectra of (**b**) W 4*f*, (**c**) Zn 2*p*, and (**d**) O 1*s* of $Ru_1W_{0.14}Zn_{1.47}O_x$. and $Ru_1W_{0.33}Zn_{1.14}O_x$, respectively.

### 3.2. Electrochemical Characterization

The electrochemical HOR performances of the catalysts were evaluated using a rotating disk electrode in a three-electrode system (Figure 7) in $H_2$-saturated 0.1 M KOH.
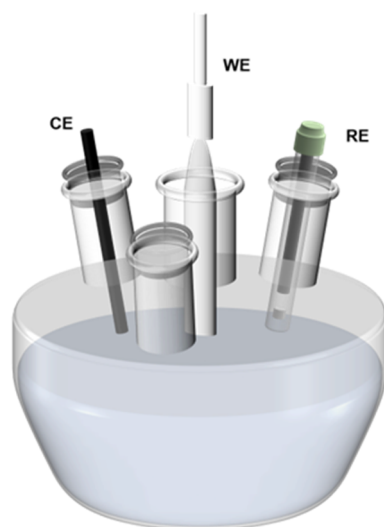


**Figure 7.** Schematic illustration of the three-electrode system.

The HOR polarization curves of the catalysts were obtained through LSV tests conducted at a rotating speed of 1600 rpm with a scan rate of 1 mV s$^{-1}$. Figure 8a shows that the $Ru_1W_{0.14}Zn_{1.47}O_x$ catalyst exhibits a higher anode current density compared to $RuZn_xO_y$, commercial Ru/C, and Pt/C. For commercial Ru/C, the catalyst loading was adjusted to 0.5 mg cm$^{-2}$ to prepare a well-dispersed catalyst membrane on the working electrode. The result suggests that the introduction of W is essential for enhancing HOR activity. However, the electrochemical performance decreases when there is an excessive amount of W, indicating that an excessive usage of W might cover the active sites of Ru and reduce the porosity of the composites, thus hindering $H_2$ transfer and decreasing the electrochemical performance. The geometric current density ($j_g$) of $Ru_1W_{0.14}Zn_{1.47}O_x$ increases rapidly at around 0 V vs. RHE compared to $RuZn_xO_y$, commercial Pt/C, and Ru/C, as confirmed by the micro-polarization region ($-5$ to 5 mV) analysis (Figure 8b). The exchange current density ($j_0$) of $Ru_1W_{0.14}Zn_{1.47}O_x$ was calculated as 1.54 mA cm$^{-2}$ in the micro-polarization region using the Butler–Volmer equation, which is 1.32 and 2.03 times higher than that of commercial Pt/C and Ru/C, respectively. The Cu-UPD analysis showed that the ECSA of $Ru_1W_{0.14}Zn_{1.47}O_x$ reached 116 m$^2$ g$^{-1}$ (Figure 8c). After normalization by ECSA, the specific activity ($j_{0,s}$) of $Ru_1W_{0.14}Zn_{1.47}O_x$ was found to be 0.026 mA cm$_{ECSA}^{-2}$, close to that of the commercial Ru/C catalyst [34]. This suggests that the enhanced HOR activity of $Ru_1W_{0.14}Zn_{1.47}O_x$ can be attributed to the favorable structure created, which has abundant exposed active sites. The polarization curves of $Ru_1W_{0.14}Zn_{1.47}O_x$ at various rotation speeds, ranging from 400 to 2500 rpm, showing that the anodic current densities consistently increase with the higher rotation speeds (Figure 8d). The Koutecký–Levich plot at an overpotential of 50 mV reveals a linear relationship between $j^{-1}$ and $\omega^{-1/2}$.

The slope of $Ru_1W_{0.14}Zn_{1.47}O_x$ is 11.1 cm$^2$ mA$^{-1}$ rpm$^{-1/2}$, which is close to the theoretical value of 14.8 cm$^2$ mA$^{-1}$ rpm$^{-1/2}$, confirming that the current is mainly derived from the HOR process involving a $2e^-$ transfer (inset of Figure 8d). The Tafel plots (Figure 8e) further demonstrate that the introduction of W significantly promotes the HOR process in alkali. The $Ru_1W_{0.14}Zn_{1.47}O_x$ catalyst exhibits the highest $j_0$ and $j_g$ at 50 mV vs. RHE compared to commercial Pt/C, Ru/C, and $RuZn_xO_y$, as shown in Figure 8f. Using the Koutecký–Levich equation, we obtained a geometric kinetic current density ($j_k$) of 7.69 mA cm$^{-2}$ for the $Ru_1W_{0.14}Zn_{1.47}O_x$ catalyst, which is 1.82 times higher than that of commercial Pt/C, and similar to that of Ru/C, despite the Ru/C loading being approximately 2.63 times higher than that of $Ru_1W_{0.14}Zn_{1.47}O_x$. The mass content of Ru in $Ru_1W_{0.14}Zn_{1.47}O_x$ and

$RuZnO_x$ nanocages has been determined to be approximately 4.5 wt% by ICP-MS. The mass activity ($j_{k,m}$) was obtained by normalizing the kinetic current density with respect to the mass of noble metal. As shown in Figure 8g, the $j_{k,m}$ of $Ru_1W_{0.14}Zn_{1.47}O_x$ catalyst is 0.9 mA $\mu g^{-1}$ at 50 mV vs. RHE, which is 1.22, 8.18, and 3.04 times higher than that of $RuZnO_x$, commercial Pt/C, and Ru/C, respectively. Furthermore, the value of $j_{k,m}$ for the $Ru_1W_{0.14}Zn_{1.47}O_x$ catalyst indicates the enhanced catalytic activity compared to other reported HOR electrocatalysts in alkaline media (Figure 8h).
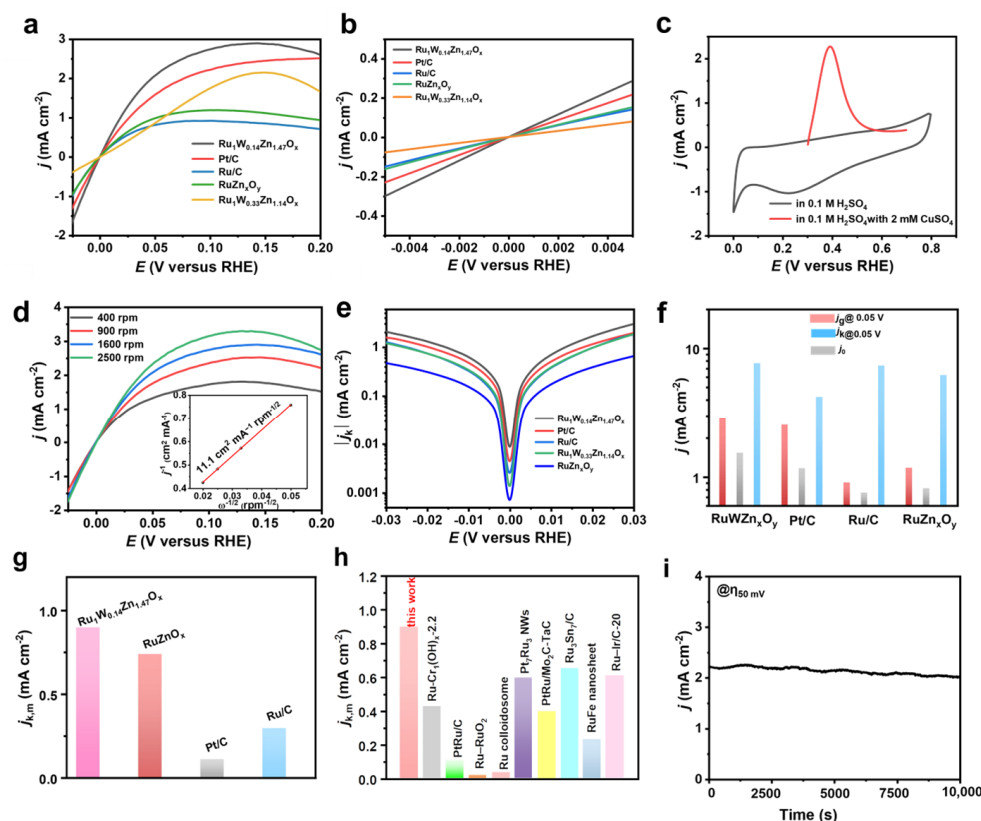


**Figure 8.** Electrocatalytic HOR performances. (**a**) Polarization curves of $Ru_1W_{0.14}Zn_{1.47}O_x$, Pt/C, Ru/C, $RuZn_xO_y$, and $Ru_1W_{0.33}Zn_{1.14}O_x$, respectively, in $H_2$-saturated 0.1 M KOH solution. (**c**) The $Cu_{upd}$ stripping voltammogram of $Ru_1W_{0.14}Zn_{1.47}O_x$. The loading of Ru is about 10 µg. (**b**) Micropolarization region between −5 to 5 mV vs. RHE of the corresponding catalysts. (**d**) Polarization curves of $Ru_1W_{0.14}Zn_{1.47}O_x$ at different rotation rates. The Koutecky–Levich plot of $Ru_1W_{0.14}Zn_{1.47}O_x$ at an overpotential of 50 mV vs. RHE inset of (**d**). (**e**) Tafel plots present the kinetic current densities of $Ru_1W_{0.14}Zn_{1.47}O_x$, Pt/C, Ru/C, $RuZn_xO_y$, and $Ru_1W_{0.33}Zn_{1.14}O_x$, respectively, derived from the Butler–Volmer equation fitting. (**f**) Comparison of the $j_g$, $j_k$, and $j_0$ of $Ru_1W_{0.14}Zn_{1.47}O_x$, $RuZn_xO_y$, Pt/C, and Ru/C at 50 mV vs. RHE. (**g**) Comparison of mass normalized current density for $Ru_1W_{0.14}Zn_{1.47}O_x$, $RuZnO_x$, commercial Pt/C, and Ru/C. (**h**) Comparison of the $j_{k,m}$ at an overpotential of 50 mV vs. RHE for $Ru_1W_{0.14}Zn_{1.47}O_x$ in this work with other alkaline HOR catalysts. The column diagrams are duplicated from the literature: $Ru$-$Cr_1(OH)_{x}$-2.2 ([35]), PtRu/C ([36]), $Ru$–$RuO_2$ ([37]), Ru colloidosome ([14]), $Pt_7Ru_3$ NWs ([12]), PtRu/$Mo_2$C-TaC ([38]), $Ru_3Sn_7$/C ([5]), RuFe nanosheet ([39]), Ru–Ir/C-20 ([11]). (**i**) Chronoamperometry (*j-t*) response of $Ru_1W_{0.14}Zn_{1.47}O_x$ in $H_2$-saturated 0.1 M KOH solution at 50 mV vs. RHE. The loading of Ru is 8.55 µg $cm^{-2}$ in all electrocatalytic tests, except Cu-UPD testing.

Besides HOR activity, operating stability is another important factor for application. Therefore, we conducted a stability test using chronoamperometry at a constant potential of 50 mV vs. RHE in $H_2$-saturated 0.1 M KOH. Figure 8i shows that the HOR current density of the $Ru_1W_{0.14}Zn_{1.47}O_x$ catalyst remains stable without noticeable decay over 10,000 s.

These results demonstrate the excellent HOR activity and stability of the $Ru_1W_{0.14}Zn_{1.47}O_x$ catalyst in alkali, suggesting its potential application in future AEMFCs.

## 4. Conclusions

In summary, we have synthesized a series of Ru-W-Zn-O nanocage composites via hydrothermal and annealing treatments using ZIF-8 as the template. The noble metal loading of the $Ru_1W_{0.14}Zn_{1.47}O_x$ catalyst is only 4.5 wt%, which has greatly reduced the cost of the anode material. Meanwhile, the optimized $Ru_1W_{0.14}Zn_{1.47}O_x$ nanocage catalyst, with a moderate amount of W, exhibits a high electrochemical surface area of 116 $m^2\ g^{-1}$ and excellent HOR activity, with a mass activity of 0.9 mA $\mu g^{-1}$ at an overpotential of 50 mV, surpassing that of commercial Pt/C and Ru/C. The high catalytic activity is primarily attributed to the incorporation of W, which modulates the d-band structure of Ru and optimizes the binding ability between active sites and intermediates. Moreover, the three-dimensional hollow porous structure promotes mass transfer and diffusion, accelerating $H_2$ transfer and improving the electrocatalytic performance. Our work presents a high-performance Pt-free catalyst material for alkaline HOR and offers valuable insights for developing highly active electrocatalysts.

**Author Contributions:** Conceptualization, X.S.; methodology, X.S.; validation, X.S.; investigation, X.S., Z.C., H.L. and S.C.; resources, Y.-R.Z.; data curation, X.S.; writing—original draft preparation, X.S. and Z.C.; writing—review and editing, Y.-R.Z.; supervision, Y.-R.Z.; project administration. All authors have read and agreed to the published version of the manuscript.

**Data Availability Statement:** The data presented in this study are available on request from the corresponding author.

**Conflicts of Interest:** The authors declare no conflicts of interest.

## References

1. Zhang, X.; Xiao, X.; Chen, J.; Liu, Y.; Pan, H.; Sun, W.; Gao, M. Toward the fast and durable alkaline hydrogen oxidation reaction on ruthenium. *Energy Environ. Sci.* **2022**, *15*, 4511–4526. [CrossRef]
2. Xue, Y.; Shi, L.; Liu, X.; Fang, J.; Wang, X.; Setzler, B.P.; Zhu, W.; Yan, Y.; Zhuang, Z. A highly-active, stable and low-cost platinum-free anode catalyst based on RuNi for hydroxide exchange membrane fuel cells. *Nat. Commun.* **2020**, *11*, 5651. [CrossRef] [PubMed]
3. Lu, Y.; Cai, Y.; Souamy, L.; Song, X.; Zhang, L.; Wang, J. Solid oxide fuel cell technology for sustainable development in China: An over-view. *Int. J. Hydrog. Energy* **2018**, *43*, 12870–12891. [CrossRef]
4. Yang, Z.; Lai, W.; He, B.; Wang, J.; Yu, F.; Liu, Q.; Liu, M.; Zhang, S.; Ding, W.; Lin, Z.; et al. Tailoring Interfacial Chemistry of Defective Carbon-Supported Ru Catalyst Toward Efficient and CO-Tolerant Alkaline Hydrogen Oxidation Reaction. *Adv. Energy Mater.* **2023**, *13*, 2300881. [CrossRef]
5. Su, L.; Fan, X.; Jin, Y.; Cong, H.; Luo, W. Hydroxyl-Binding Energy-Induced Kinetic Gap Narrowing between Acidic and Alkaline Hydrogen Oxidation Reaction on Intermetallic $Ru_3Sn_7$ Catalyst. *Small* **2023**, *19*, 2207603. [CrossRef] [PubMed]
6. Su, L.; Jin, Y.; Gong, D.; Ge, X.; Zhang, W.; Fan, X.; Luo, W. The Role of Discrepant Reactive Intermediates on Ru-Ru2P Heterostructure for pH-Universal Hydrogen Oxidation Reaction. *Angew. Chem. Int. Ed.* **2022**, *62*, 2215585.
7. Wang, P.; Wang, C.; Yang, Y.; Chen, S.; Cheng, Z.; Huang, M.; Tong, H.; Chen, Q. RuP Nanoparticles Supported on N, O Codoped Porous Hollow Carbon for Efficient Hydrogen Oxidation Reaction. *Adv. Mater. Interfaces* **2022**, *9*, 2102193. [CrossRef]
8. Zhou, Y.; Xie, Z.; Jiang, J.; Wang, J.; Song, X.; He, Q.; Ding, W.; Wei, Z. Lattice-confined Ru clusters with high CO tolerance and activity for the hydrogen oxidation reaction. *Nat. Catal.* **2020**, *3*, 454–462. [CrossRef]
9. Mao, J.; He, C.-T.; Pei, J.; Liu, Y.; Li, J.; Chen, W.; He, D.; Wang, D.; Li, Y. Isolated Ni Atoms Dispersed on Ru Nanosheets: High-Performance Electrocatalysts toward Hydrogen Oxidation Reaction. *Nano Lett.* **2020**, *20*, 3442–3448. [CrossRef]
10. Cui, Y.; Xu, Z.; Chen, D.; Li, T.; Yang, H.; Mu, X.; Gu, X.; Zhou, H.; Liu, S.; Mu, S. Trace oxophilic metal induced surface reconstruction at buried RuRh cluster interfaces possesses extremely fast hydrogen redox kinetics. *Nano Energy* **2021**, *90*, 106579. [CrossRef]
11. Ohyama, J.; Kumada, D.; Satsuma, A. Improved hydrogen oxidation reaction under alkaline conditions by ruthenium–iridium alloyed nanoparticles. *J. Mater. Chem. A* **2016**, *4*, 15980–15985. [CrossRef]
12. Scofield, M.E.; Zhou, Y.; Yue, S.; Wang, L.; Su, D.; Tong, X.; Vukmirovic, M.B.; Adzic, R.R.; Wong, S.S. Role of Chemical Composition in the Enhanced Catalytic Activity of Pt-Based Alloyed Ultrathin Nanowires for the Hydrogen Oxidation Reaction under Alkaline Conditions. *ACS Catal.* **2016**, *6*, 3895–3908. [CrossRef]

13. Qin, B.; Yu, H.; Gao, X.; Yao, D.; Sun, X.; Song, W.; Yi, B.; Shao, Z. Ultrathin IrRu nanowire networks with high performance and durability for the hydrogen oxidation reaction in alkaline anion exchange membrane fuel cells. *J. Mater. Chem. A* **2018**, *6*, 20374–20382. [CrossRef]

14. Yang, X.; Ouyang, B.; Shen, P.; Sun, Y.; Yang, Y.; Gao, Y.; Kan, E.; Li, C.; Xu, K.; Xie, Y. Ru Colloidosome Catalysts for the Hydrogen Oxidation Reaction in Alkaline Media. *J. Am. Chem. Soc.* **2022**, *144*, 11138–11147. [CrossRef] [PubMed]

15. Ming, M.; Zhang, Y.; He, C.; Zhao, L.; Niu, S.; Fan, G.; Hu, J.S. Room-Temperature Sustainable Synthesis of Selected Platinum Group Metal (PGM = Ir, Rh, and Ru) Nanocatalysts Well-Dispersed on Porous Carbon for Efficient Hydrogen Evolution and Oxidation. *Small* **2019**, *15*, 1903057. [CrossRef] [PubMed]

16. Wang, L.; Xu, Z.; Kuo, C.H.; Peng, J.; Hu, F.; Li, L.; Chen, H.Y.; Wang, J.; Peng, S. Stabilizing Low-Valence Single Atoms by Constructing Metalloid Tungsten Carbide Supports for Efficient Hydrogen Oxidation and Evolution. *Angew. Chem. Int. Ed.* **2023**, *62*, 2311937.

17. Jiang, J.; Tao, S.; He, Q.; Wang, J.; Zhou, Y.; Xie, Z.; Ding, W.; Wei, Z. Interphase-oxidized ruthenium metal with half-filled d-orbitals for hydrogen oxidation in an alkaline solution. *J. Mater. Chem. A* **2020**, *8*, 10168–10174. [CrossRef]

18. Yang, F.; Wang, Y.; Cui, Y.; Yang, X.; Zhu, Y.; Weiss, C.M.; Li, M.; Chen, G.; Yan, Y.; Gu, M.D.; et al. Sub-3 nm Pt@Ru toward Outstanding Hydrogen Oxidation Reaction Performance in Alkaline Media. *J. Am. Chem. Soc.* **2023**, *145*, 27500–27511. [CrossRef] [PubMed]

19. Ohyama, J.; Sato, T.; Yamamoto, Y.; Arai, S.; Satsuma, A. Size Specifically High Activity of Ru Nanoparticles for Hydrogen Oxidation Reaction in Alkaline Electrolyte. *J. Am. Chem. Soc.* **2013**, *135*, 8016–8021. [CrossRef]

20. He, S.; Tu, Y.; Zhang, J.; Zhang, L.; Ke, J.; Wang, L.; Du, L.; Cui, Z.; Song, H. Ammonia-Induced FCC Ru Nanocrystals for Efficient Alkaline Hydrogen Electrocatalysis. *Small* **2023**, *20*, 08053. [CrossRef]

21. Li, Y.; Yang, C.; Yue, J.; Cong, H.; Luo, W. Polymorphism-Interface-Induced Work Function Regulating on Ru Nanocatalyst for Enhanced Alkaline Hydrogen Oxidation Reaction. *Adv. Funct. Mater.* **2023**, *33*, 11586. [CrossRef]

22. Mahmood, J.; Li, F.; Jung, S.-M.; Okyay, M.S.; Ahmad, I.; Kim, S.-J.; Park, N.; Jeong, H.Y.; Baek, J.-B. An efficient and pH-universal ruthenium-based catalyst for the hydrogen evolution reaction. *Nat. Nanotechnol.* **2017**, *12*, 441–446. [CrossRef] [PubMed]

23. Zhuang, Z.W.; Wang, Y.; Xu, C.Q.; Liu, S.J.; Chen, C.; Peng, Q.; Zhuang, Z.B.; Xiao, H.; Pan, Y.; Lu, S.Q.; et al. Three-dimensional open nano-netcage electrocatalysts for efficient pH-universal overall water splitting. *Nat. Commun.* **2019**, *10*, 4875. [CrossRef] [PubMed]

24. Li, Y.Z.; Abbott, J.; Sun, Y.C.; Sun, J.M.; Du, Y.C.; Han, X.J.; Wu, G.; Xu, P. Ru nanoassembly catalysts for hydrogen evolution and oxidation reactions in electrolytes at various pH values. *Appl. Catal. B-Environ. Energy* **2019**, *258*, 117952. [CrossRef]

25. Wu, Y.H.; Li, Y.W.; Gao, J.K.; Zhang, Q.C. Recent advances in vacancy engineering of metal-organic frameworks and their derivatives for electrocatalysis. *Sus. Mat.* **2021**, *1*, 66–87. [CrossRef]

26. Li, G.D.; Zhao, S.L.; Zhang, Y.; Tang, Z.Y. Metal-Organic Frameworks Encapsulating Active Nanoparticles as Emerging Composites for Catalysis: Recent Progress and Perspectives. *Adv. Mater.* **2018**, *30*, 1800702. [CrossRef] [PubMed]

27. Duan, J.J.; Chen, S.; Li, Y.B.; Zhao, C. Closely Arranged 3D-0D Graphene-Nickel Sulfide Superstructures for Bifunctional Hydrogen Electrocatalysis. *ACS Appl. Energy Mater.* **2018**, *1*, 6368–6373. [CrossRef]

28. Zhu, J.; Chen, F.; Zhang, Z.; Li, M.; Yang, Q.; Yang, Y.; Bao, Z.; Ren, Q. M-Gallate (M = Ni, Co) Metal–Organic Framework-Derived Ni/C and Bimetallic Ni–Co/C Catalysts for Lignin Conversion into Monophenols. *ACS Sustain. Chem. Eng.* **2019**, *7*, 12955–12963. [CrossRef]

29. Ma, M.; Chen, C.; Zhang, X.; Zhao, H.; Wang, Q.; Du, G.; Xie, Z.; Kuang, Q. Mo-modified electronic effect on sub-2 nm Ru catalyst for enhancing hydrogen oxidation catalysis. *J. Mater. Chem. A* **2023**, *11*, 10807–10812. [CrossRef]

30. Qiu, Z.; Li, Y.; Gao, Y.; Meng, Z.; Sun, Y.; Bai, Y.; Suen, N.T.; Chen, H.C.; Pi, Y.; Pang, H. 2D MOF-assisted Pyrolysis-displacement-alloying Synthesis of High-entropy Alloy Nanoparticles Library for Efficient Electrocatalytic Hydrogen Oxidation. *Angew. Chem. Int. Ed.* **2023**, *62*, 2306881. [CrossRef]

31. Lao, M.M.; Zhao, G.Q.; Li, P.; Ma, T.Y.; Jiang, Y.Z.; Pan, H.G.; Dou, S.X.; Sun, W.P. Manipulating the Coordination Chemistry of Ru-N(O)-C Moieties for Fast Alkaline Hydrogen Evolution Kinetics. *Adv. Funct. Mater.* **2021**, *31*, 2100698. [CrossRef]

32. Han, P.; Yang, X.; Wu, L.; Jia, H.; Chen, J.; Shi, W.; Cheng, G.; Luo, W. A Highly-Efficient Boron Interstitially Inserted Ru Anode Catalyst for Anion Exchange Membrane Fuel Cells. *Adv. Mater.* **2023**, *36*, 2304496. [CrossRef]

33. Yang, Y.; Shao, X.; Zhou, S.; Yan, P.; Isimjan, T.T.; Yang, X. Interfacial Electronic Coupling of NC@$WO_3$-$W_2$C Decorated Ru Clusters as a Reversible Catalyst toward Electrocatalytic Hydrogen Oxidation and Evolution Reactions. *ChemSusChem* **2021**, *14*, 2992–3000. [CrossRef] [PubMed]

34. Feng, Y.; Lu, S.; Fu, L.; Yang, F.; Feng, L. Alleviating the competitive adsorption of hydrogen and hydroxyl intermediates on Ru by d–p orbital hybridization for hydrogen electrooxidation. *Chem. Sci.* **2024**, *15*, 2123–2132. [CrossRef] [PubMed]

35. Zhang, B.X.; Zhang, B.H.; Zhao, G.Q.; Wang, J.M.; Liu, D.Q.; Chen, Y.P.; Xia, L.X.; Gao, M.X.; Liu, Y.F.; Sun, W.P.; et al. Atomically dispersed chromium coordinated with hydroxyl clusters enabling efficient hydrogen oxidation on ruthenium. *Nat. Commun.* **2022**, *13*, 5894. [CrossRef] [PubMed]

36. Zhan, C.; Xu, Y.; Bu, L.; Zhu, H.; Feng, Y.; Yang, T.; Zhang, Y.; Yang, Z.; Huang, B.; Shao, Q.; et al. Sub nanometer high-entropy alloy nanowires enable remarkable hydrogen oxidation catalysis. *Nat. Commun.* **2021**, *12*, 6261. [CrossRef] [PubMed]

37.  Zhang, X.B.; Xia, L.X.; Zhao, G.Q.; Zhang, B.X.; Chen, Y.P.; Chen, J.; Gao, M.X.; Jiang, Y.Z.; Liu, Y.F.; Pan, H.G.; et al. Fast and Durable Alkaline Hydrogen Oxidation Reaction at the Electron-Deficient Ruthenium-Ruthenium Oxide Interface. *Adv. Mater.* **2023**, *35*, 2208821. [CrossRef] [PubMed]

38.  Hamo, E.R.; Singh, R.K.; Douglin, J.C.; Chen, S.; Hassine, M.B.; Carbo-Argibay, E.; Lu, S.; Wang, H.; Ferreira, P.J.; Rosen, B.A.; et al. Carbide-Supported PtRu Catalysts for Hydrogen Oxidation Reaction in Alkaline Electrolyte. *ACS Catal.* **2021**, *11*, 932–947. [CrossRef]

39.  Li, Y.B.; Yang, C.Y.; Ge, C.X.; Yao, N.; Yin, J.L.; Jiang, W.Y.; Cong, H.J.; Cheng, G.Z.; Luo, W.; Zhuang, L. Electronic Modulation of Ru Nanosheet by d-d Orbital Coupling for Enhanced Hydrogen Oxidation Reaction in Alkaline Electrolytes. *Small* **2022**, *18*, 2202404. [CrossRef]